On-the-fly Non-adiabatic Dynamics Simulations of Single-Walled Carbon Nanotubes with Covalent Defects

Braden M. Weight[1,2], Andrew E. Sifain[3], Brendan J. Gifford[2], Han Htoon[2], and Sergei Tretiak[2*]

[1]*Department of Physics and Astronomy, University of Rochester, Rochester, NY 14627, U.S.A*

[2]*Center for Integrated Nanotechnologies, Center for Nonlinear Studies, and Theoretical Division Los Alamos National Laboratory, Los Alamos, NM 87545, U.S.A.*

[3]*Department of Chemistry, Princeton University, Princeton, NJ 08540 U.S.A.*

Email: serg@lanl.gov

ABSTRACT

Single-walled carbon nanotubes (SWCNTs) with covalent surface defects have been explored recently due to their promise for use in single-photon telecommunication emission and in spintronic applications. The dynamical evolution of excitons (the primary electronic excitations) in these systems has only been loosely explored due to the limitations of these large systems (> 300 atoms). We present computational modeling of non-radiative relaxation on a variety of SWCNT chiralities with single-defect functionalization schemes. Our modeling uses a trajectory surface hopping algorithm accounting for excitonic effects with a configuration interaction approach. We find a strong chirality and defect-composition dependence on the population relaxation (50 – 500 fs) between the nanotube band-gap excitation and the defect-associated, single-photon-emitting state, giving insight into the dynamic trapping nature of these localized excitonic states. Engineering fast population decay into the quasi-two-level sub-system with weak coupling to higher-energy states increases the effectiveness and controllability of these quantum light emitters.

TOC Figure:
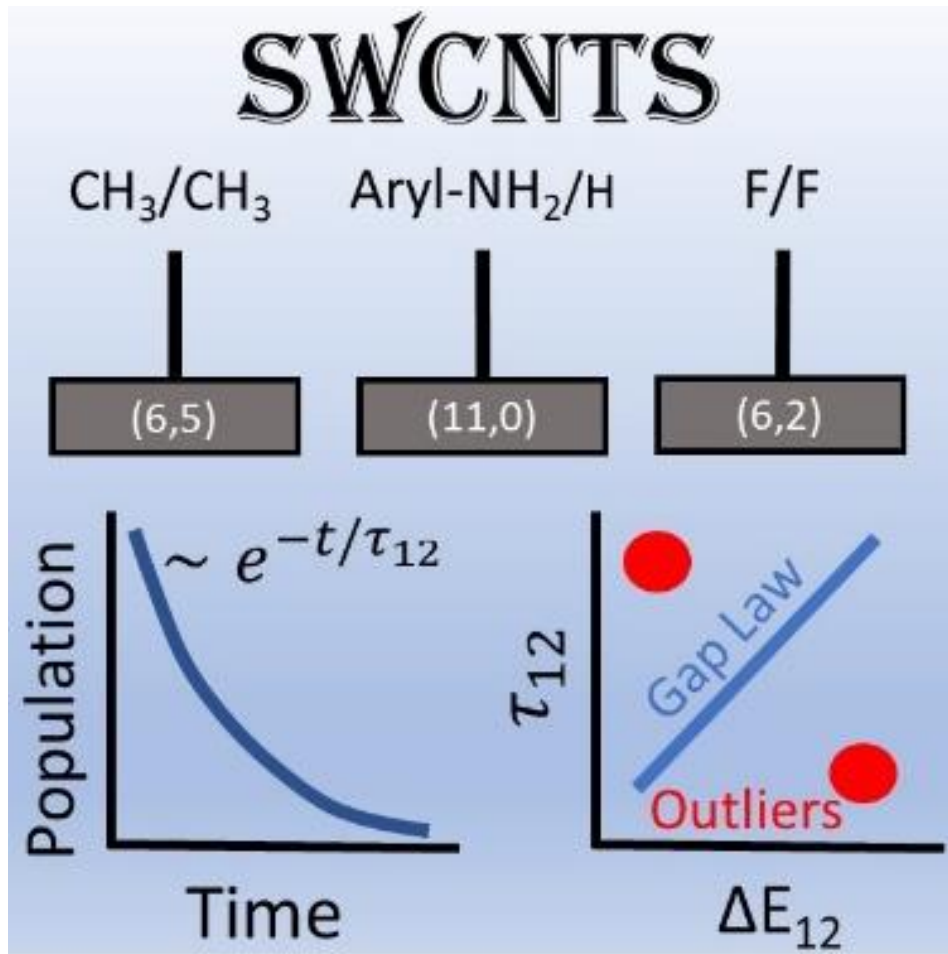
Single walled carbon nanotubes (SWCNTs) functionalized with a single[1–11] or multiple[12–15] sp^3-hybridized defects (each consisting of a covalent bond of two groups on a single carbon ring) are regarded as excellent sources of single photons at room temperature.[4,16,17] This makes them useful for applications in quantum circuits as well as in telecommunications[16] and other technologies relying on highly tunable single-photon emission. Much recent theoretical work has been done exploring the structure-electronic property relationships in these systems from the point of view of the Frank-Condon geometry.[1–3,7,10,12] However, control over the dynamical processes following electronic excitation has only loosely been discussed from the theoretical side.[18–24] A better understanding of these processes, such as carrier trapping and detrapping,[5,14] auger recombination[20,21] and exciton redistribution/diffusion,[5,14,25] would give insight into further tunability and control of these systems' optical and spintronic properties.[26–28] Recent experimental results characterizing the photoluminescence dynamics[5,14,25] in these systems inspires state-of-the-art simulations. In this study, we explore nonradiative relaxation processes in a variety of SWCNT chiralities and single-defect functionalization chemistries to elucidate the structure-dependent tunability of the exciton relaxation into the energetically low-lying emitting state associated with the defect.
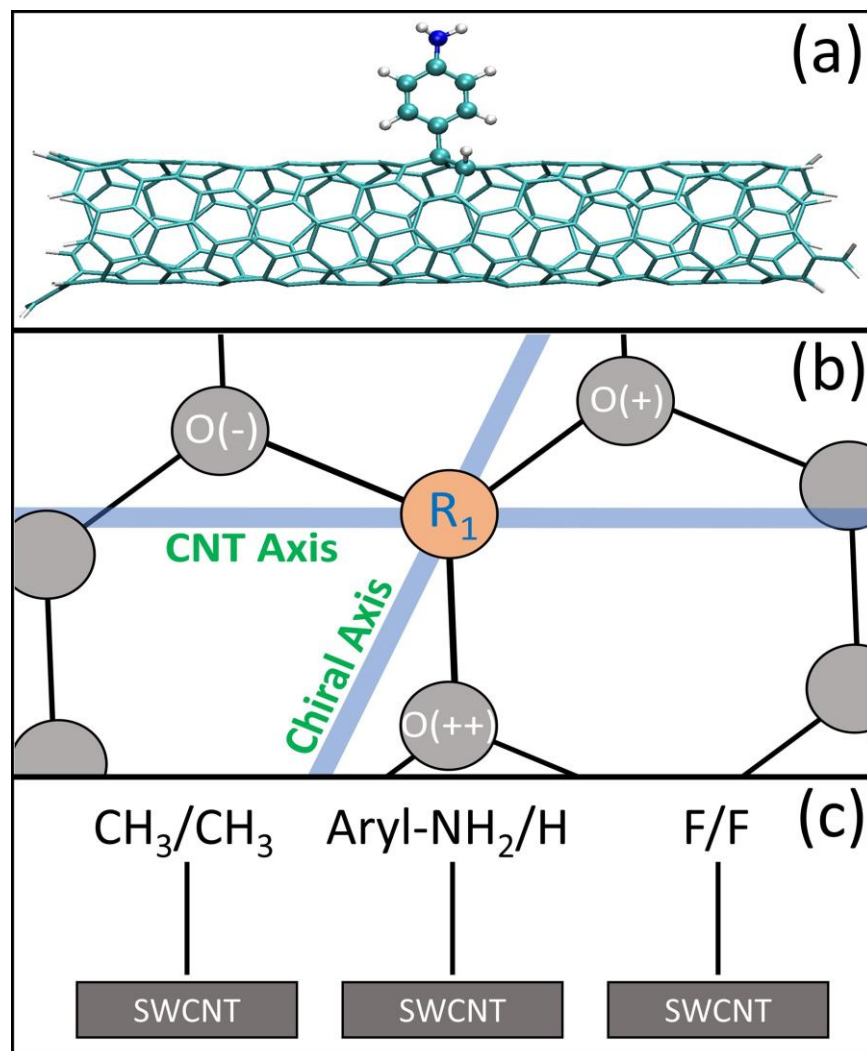

4

Fig. 1: (a) (6,2) SWCNT with Aryl-NH$_2$/H defect in the Ortho(-) configuration. (b) Definition of the defect configuration with respect to the tube and chiral axes. (c) Chemical species used as chemical adducts in this work.

SWCNT chirality and chemical species used for functionalization effects the optoelectronic characteristics of the material. As such, we constructed a set of SWCNTs with differing chiralities – (6,2), (6,5), (11,0) – and resulting differing diameters (0.57, 0.75, and 0.86 nm) and chiral angles (14, 27, and 0°). These pristine species are functionalized with a set of chemical adducts – F/F, CH$_3$/CH$_3$, Aryl-NH$_2$/H – focusing on the most experimentally relevant *ortho* binding configurations – *ortho*(++) and *ortho*(-) for these chiralities where *ortho* indicates that the set of covalent attachments are bonded to adjacent carbon atoms (see Fig. 1 and Methods in Supplemental Information). From our previous studies,[2,3,7,10] the binding configuration of the defect, uniquely defined by their the angle between the vector between the two functionalized carbon atoms and the tube axis has the largest control over the emission energy. The low-lying defect state (denoted as E_{11}^*) can be energetically lower than the lowest fundamental excitonic band of the nanotube E_{11} by 100 – 400 meV. The chosen configuration's redshift depends uniquely on the SWCNT chirality [specifically the mod(n-m,3) value][3]. Changing the functional group has a much smaller effect (10 – 100 meV).[1,7] We note that the charge on the sp^3-hybridized SWCNT atom connected directly to the defect and the hybridization of the bonding defect atom correlates with the amount of redshift of the defect exciton from the pristine E_{11} exciton,[1,6,7] which implies that strongly electron-withdrawing groups such as direct fluorine attachment (denoted as F/F or 2F in this work) typically provide the lowest-energy E_{11}^* excitation.

Previous experimental work[5,14] has suggested that strong thermal de-trapping and exciton redistribution processes are prevalent prior to emission on time-scales similar to the expected non-radiative relaxation. In designing ideal quantum emitters with useful properties – such as small spectral linewidths and large energetic separation between the lowest emitting excited state S_1 and higher electronic levels – dynamical control of the non-radiative relaxation into the S_1 state is fundamentally required. In this work, we show that such control is possible through choice of SWCNT chirality as well as defect configuration and chemical composition by a modulation of the excitonic relaxation rate from the E_{11} band-edge state to the low-lying E_{11}^* (S_1) exciton. Our results showcase a tunable single-exponential decay constant τ_{12} that varies from 60 to 450 fs through experimentally simple changes to the SWCNT chirality and functional group chemistry, where the changes in population dynamics are shown to stem from strong changes in non-adiabatic coupling throughout the trajectories.
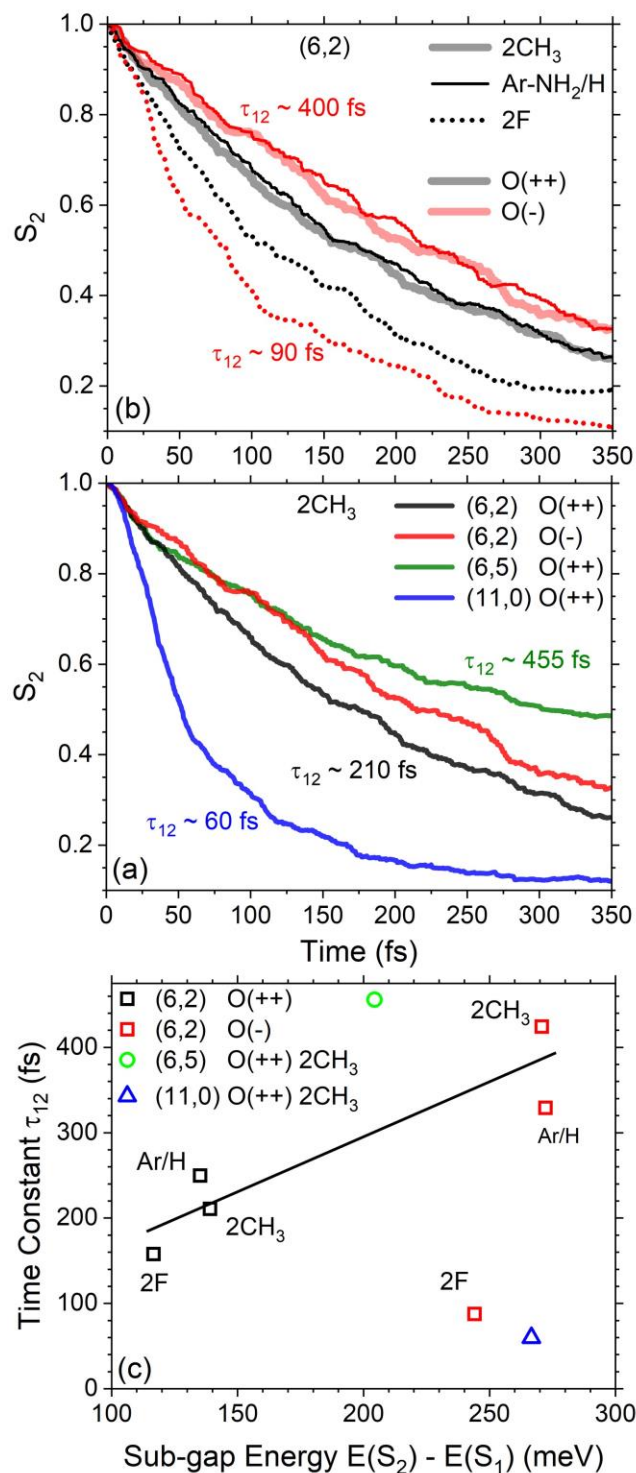
Fig. 2: (a) Population dynamics for a set of SWCNT chiralities ((6,2), (11,0), and (6,5)) and two defect configurations for the (6,2) chirality (Ortho(++) and Ortho(-)). (b) Chemical composition dependence in the (6,2) chirality with 2CH₃ (bold), Aryl-NH₂/H (solid), and 2F (dotted) as chemical adducts. (c) Dependence of the relaxation time constant τ_{12}, given by a single exponential fit, on the sub-gap energy between electronic states S_1 and S_2 evaluated at the ground state minimum geometry.

The non-adiabatic excited state molecular dynamics (NEXMD) software package[29,30] [‡] has been used for all simulations presented in this work, and computational methodology is presented in Methods in Supplemental Information. Briefly, after performing Born–Oppenheimer dynamics at room temperature to produce conformational samples of the geometry in the ground state, a set of non-adiabatic trajectories were initialized in the second singlet electronic state S_2 (which possesses the character/energy of the E_{11} band-edge exciton, see Supplemental Figs S1-S3 for absorption spectra). The nuclear and electronic degrees of freedom (DOFs) were propagated in time according to the trajectory surface hopping (TSH) method[31] as implemented in NEXMD with excitonic effects considered at the configuration interaction singles (CIS) level. The state population was computed at each time step and averaged across 300 trajectories for each system to evaluate relaxation rates by fitting the S_2 population to a single-exponential $P_2(t) \sim e^{-t/\tau_{12}}$ (Fig. 2a,b, see Supplemental Figs S4 and S5 for convergence with number of trajectories and brief discussion on higher excited states and the S_2-to-S_1 rate-limiting step, respectively). A strong dependence on chirality (Fig. 2a) is seen between the (11,0), (6,2), and (6,5) SWCNTs with increasing single-exponential relaxation time τ_{12} = 60, 210, and 455 fs, respectively, where each system was functionalized with $2CH_3$ in the *ortho*(++) configuration. This choice of functional species was explored in previous studies[1,7,12] and provides a functional species that should have a minimal impact on the SWCNT aside from the sp^3-hybridization, in contrast to another type of defect which may have large charge induction, such as 2F, as will be explored later. This dependence cannot be attributed to diameter since (6,2) has the smallest diameter, followed by (6,5) and (11,0). The chiral angle is likely the dominating factor, since the zig-zag (11,0) relaxes much faster than the chiral (6,5) and (6,2). We note that direct comparison between chiralities given the same functionalization configuration is difficult since each SWCNT has distinct spectral features upon functionalization arising from the mod(n-m,3) value and diameter of the chirality.[3] However, (11,0) provides a comparatively fast relaxation from the higher-energy states to a quasi-two-state sub-system $\{S_0, S_1\}$ and therefore is *beneficial for use in quantum light-emitting applications to minimize thermal de-trapping events.*

Focusing on the (6,2) chirality, Figure 2b showcases the dependence of the population dynamics on the defect configuration (*ortho*(++), black; *ortho*(-), red) and composition (thick solid, $2CH_3$; thin solid, Aryl-NH_2/H; dotted, 2F). For (6,2), the *ortho*(-) configuration produces the largest redshift ($\Delta E_{11} = E_{11} - E_{11}^*$) of the S_1 defect-associated state from the pristine band-edge exciton E_{11} (see Supplemental Figs. S1-S3) and *ortho*(++) system the second largest, which is consistent with our previous work.[3] In this sense, the decay constant τ_{12} should be dependent on the electronic energy differences between excited states dictated by the configuration (i.e., non-radiative "gap law").[32] For the $2CH_3$ (Aryl-NH_2/H) adduct, *ortho*(++) and *ortho*(-) configurations produce single-exponential decay times of τ_{12} = 210 (250) and 424 (330) fs, respectively. As expected for the configuration with the larger redshift, the relaxation time is longer since the energetic gap is increased;

however, for the 2F adduct, this trend is broken with decay times of 158 and 88 fs for *ortho*(++) and *ortho*(-), respectively. We elucidate this abnormality later. For the (6,2) chirality (squares in Fig. 2c), this gap-law trend (black line) holds for the methyl and aryl adducts, but the fluorinated cases act oppositely. The (6,5) (circle) and (11,0) (triangle) chiralities act independently (i.e., with unique gap-law prefactors) from the (6,2) due to the differences in diameter and mod(n-m,3) values,[3] and one would need to explore various configurations and chemical compositions of defects on these SWCNTs to find a reasonable gap law involving these structures.
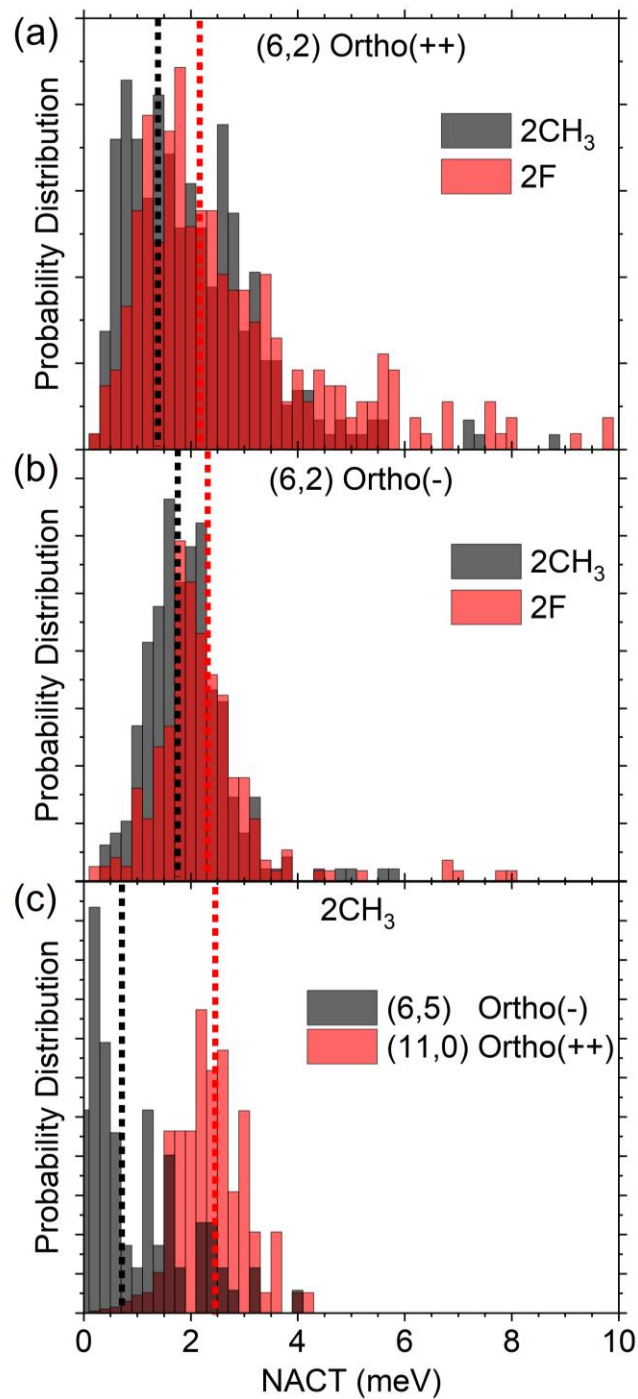
Fig. 3: Probability distributions for the magnitude of the scalar non-adiabatic coupling (NACT) at a moment of hop from S_2 to S_1. (a − b) indicate (6,2) systems with (a) Ortho(++) and (b) Ortho(-), each with $2CH_3$ (Black) and 2F (Red). (c) (6,5) (Black) and (11,0) (Red), each with $2CH_3$ in their respective Ortho(++). The vertical dashed lines indicate the mean value of the distribution.

The probability of hopping between adiabatic states is dictated by the magnitude of the scalar non-adiabatic coupling (NACT, see Methods in Supplemental Information), so systems that sample large NACT magnitudes more frequently, may exhibit faster population decay. Figure 3 shows the probability distributions of the NACT *at the moment of a hop* from S_2 to S_1 state for each system with unique population dynamics (omitting aryl adducts since they show similar trends as methyl). Examining the (6,2) structures (Fig. 3 a,b), the configuration of the defect shows varied distributions with *ortho*(++) exhibiting a much longer tail than *ortho*(-), even for the $2CH_3$ adduct (black). The long tail in the NACT should be correlated with sampling larger NACT on average and thus gives rise to faster non-radiative decay. In both configurations, the average NACT (vertical dotted lines) for the 2F (red) adduct is larger than the $2CH_3$. For the (6,5) (black) and (11,0) (red), with the two extremum population decay rates, the average NACT follows the expected trend.

The NACT distributions for the fluorinated cases suggest that the *ortho*(++) may relax faster due to the long tail; however, we find the opposite (Fig. 2b), contrary to the $2CH_3$ case. As such, we seek to understand the physical mechanism that controls the NACT throughout the trajectory in each system. To answer these questions, we turn our attention to various dynamical quantities that may relate the chemical nature of the system (i.e., charge, bond character, etc.) to the corresponding NACT quantity and population decay.
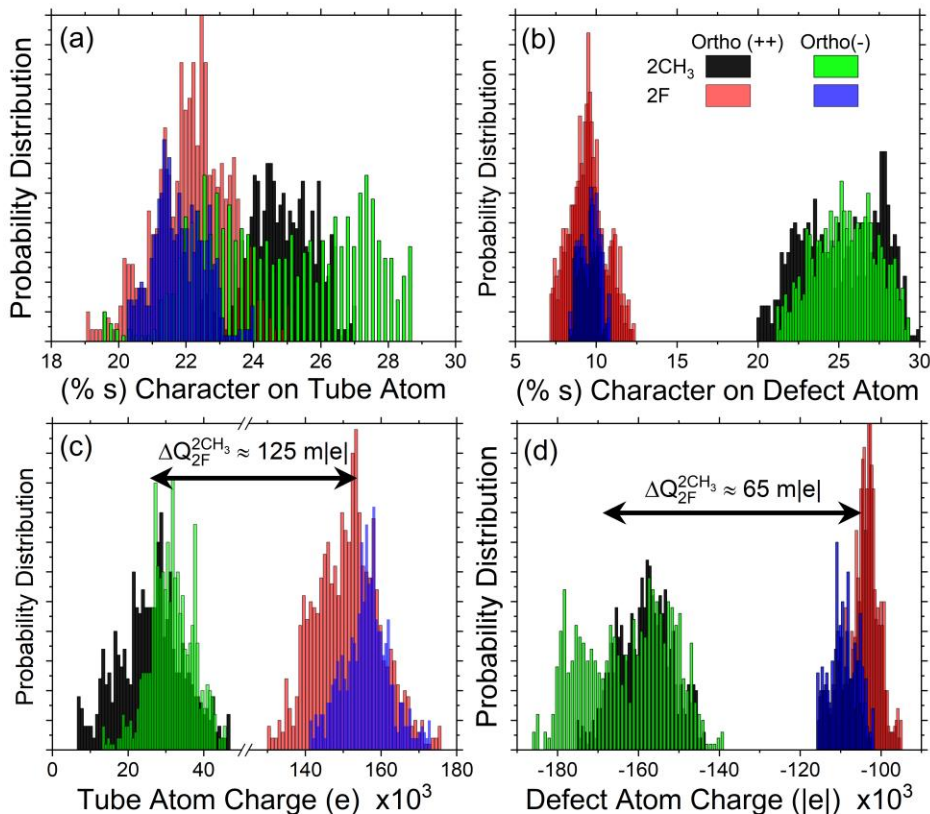

Fig. 4: Probability distributions for the (a) percent s-atomic orbital character (% s) on the SWCNT atom attached to the defect, (b) %s character on the defect atom connected to the SWCNT, (c) NBO charge on the SWCNT atom, and (d) NBO charge on the defect atom. All systems are (6,2) chirality.

Electronegative adducts are known to cause a large degree of perturbation to the local charges on the tube surface near the defect attachment.[1,6,7] This is believed to dictate the subtle redshift stemming from chemical composition of the defect; however, we posit that this redistribution of local charges drastically affects the relaxation rate through known changes to the hybridization of the SWCNT carbon atoms bonded to the defect, ultimately causing the coupling between electronic wavefunctions of the states.[1] Figure 4 shows the probability distributions of four dynamical quantities – natural bond orbital (NBO) bond character (depicted as %s) as well as the NBO charge of the SWCNT-defect interfacial atoms. Note that all systems are of (6,2) chirality. The %s character on the SWCNT atom (Fig. 4a) with the 2F adduct restricts the values to near $21 - 23$ %, while the $2CH_3$ adducts – having a more flexible bond – allow the s character to fluctuate widely between 20 and 29%. Note that 33 % indicates an sp^2-carbon. The ortho(++) (black) distribution is centered at 25% (i.e., sp^3), while the ortho(-) (green) shows bimodal nature with centers at 22 and 27%. Since all species show overlapping distributions, the %s character on the SWCNT atom may not be a reliable indicator of the population decay properties between similar defect types (i.e., methyl or aryl); however, the 2F adducts decrease the %s character. Generally, bonds involving atoms with higher p-character are less rigid since unhybridzed p-orbitals generate more rigid bonds due to increased p-orbital overlap. The higher p-character in the 2F system therefore may influence the most active vibrational modes, resulting in the increased relaxation rate. The %s character on the defect atom (covalently bonded to the SWCNT atom, Fig. 4b) shows non-overlapping distributions between C and F attachments. This indicates that the C-adduct bonds are fluctuating around sp^3-hybridization (% s $\sim$ 25 %), while the F-adduct bonds are dominated by p-atomic orbitals with contributions up to 90 % p. This property of the adduct atom is not likely to directly influence the relaxation rate, since the exciton is not spatially localized onto the adduct. Figure 4c,d shows the NBO charge on the SWCNT atom and defect atom. As noted previously, the charge on the SWCNT atom has been suggested to control the emission energy of the defect state (E_{11}^*). To be clear, here we are not interested in the radiative transition energy between E_{11}^* and ground state; rather we are interested in the non-radiative transition between E_{11} and E_{11}^*, which has not yet been correlated to the SWCNT charge. The charge on the SWCNT atom (Fig. 4c) is positive in both types of adducts, as was shown in a previous report,[7] but the probability distributions at finite temperature *for both configurations* are slightly shifted by $\sim$ 10 mili-electrons (m|e|) from one another; the *ortho*(++) configuration shows a smaller positive charge on the SWCNT atom. Moving to the charge on the defect atom (Fig. 4d), we find the opposite – but equivalent – effect, where the charge on the defect atom in the *ortho*(++) configuration shows a slightly smaller negative charge ($\sim$ 10 m|e|). We note that the charge on the defect atom in the $2CH_3$ *ortho*(-) case is again showing a bimodal distribution with centers at -180 and -155 m|e|, similar to the %s character on the SWCNT atom for the same species. This bimodal nature may be indicative of a large nuclear reorganization between the E_{11} and E_{11}^* electronic states, which will be the main point of the following discussion. The probability distributions of the sub-gap energy $E_2 - E_1$ are shown in Fig. S6 for the (6,2) chirality, which shows similar information as Fig. 2c.
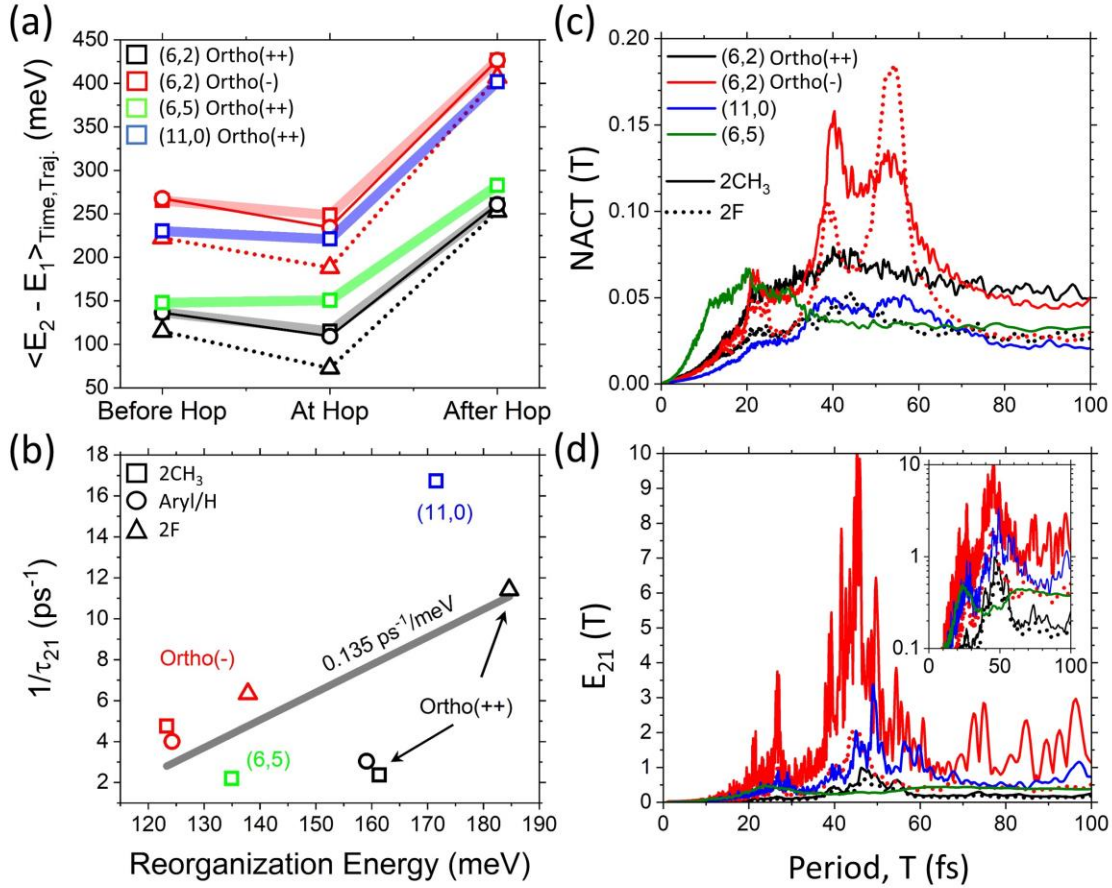
Figure 5: (a) The sub-gap energy $E_2 - E_1$ as an average over time and trajectory taken before the hop (while in S_2), at the hop (only trajectory average), and after the hop (while in S_1). (b) Rate of population transfer from S_2 to S_1 ($1/\tau_{21}$) as a function of reorganization energy at finite temperature E_R between S_2 and S_1 calculated as $E_R = <E_{21}^{After}> - <E_{21}^{Before}>$, where $<...>$ denote time and trajectory averages. A linear fit was performed on all data points, indicating a slope of 0.135 ± 0.07 ps^{-1}/meV. (c,d) Frequency distributions for two dynamical quantities: (c) non-adiabatic coupling scalar (NACT) and (d) sub-gap energy $E_2 - E_1$.

Nuclear reorganization upon electronic excitation is generally assumed to be small in rigid systems like SWCNTs[33,34] and therefore not considered as a main driving force for non-radiative decay to lower excited states. However, our calculations show that the reorganization energy between S_2 (E_{11}) and S_1 (E_{11}^*) is on the order of 150 meV, on the same order as the redshift of the defect-associated state from the band edge. Figure 5a shows the S_2/S_1 sub-gap energy averaged over time and trajectory *before*, *at*, and *after* the transition to the lower S_1 state for all species. Notably, at the transition, all species except (6,5) show a decrease in sub-gap energy, implying that the thermal fluctuations in the state energies allow for increased NACT $\sim 1/E_{21}$. The fluorinated adducts show an increased reduction in sub-gap energy at the hop, which points to *increased energetic fluctuations in the fluorinated systems*. The sub-gap energy after the transition is noticeably higher than

before the hop, which indicates a significant reorganization energy between S_1 and S_2. Figure 5b depicts the transition rate $(1/\tau_{21})$ as a function of the reorganization energy, which is then fit to a linear function with a slope of 0.135 ± 0.07 ps^{-1}/meV. The data suggests a correlation between the relaxation rate and the reorganization energy, which can be interpreted as increased sampling of a smaller energy difference between electronically excited states due to a large shift in the excited state minimum. Interestingly, Aryl/H and 2CH$_3$ share the same reorganization energy, so *the reorganization is expected to stem from the local re-distribution of charges between the excited states*, governed by the strong electronegative 2F adducts, which is evident from Fig. 4. The defect atoms themselves play little-to-no role in the reorganization (see Fig. S9 for a brief analysis of the geometric reorganization). It is important to note that the choice of sub-gap energy does not largely affect the trends shown in Fig. 2c at the Frank-Condon geometry (see Fig. S7 for comparison with non-Frank-Condon geometries).

To elucidate the direct effects on the NACT, we now examine dynamical quantities in Fourier space. Figure 5c,d shows frequency (in oscillation period) distributions of various dynamical quantities (NACT, Fig. 5c; sub-gap energy E_2-E_1, Fig. 5d). We note that the Fourier spectrum of the NACT shows widely varied localization properties between chiralities and adduct types. The two (6,2) *ortho*(-) species exhibit two large peaks near 40 – 45 and 55 fs, in addition to a weak peak near 25 fs. The latter peak can be directly attributed to C-C bond stretching throughout the SWCNT lattice (see Fig. S10a,b for Fourier representations of C-C and C-F bond lengths, respectively), while the former two peaks at higher oscillation period show that the NACTs are more strongly coupled to some slower vibronic modes. The relative heights in the two large peaks showcase the modification from the 2CH$_3$ (solid, red) to the 2F (dotted, red) adducts; the fluorination shifts the peak at 40 – 45 fs down and the peak at 55 fs up, effectively swapping the relative contributions of the two modes. However, neither mode disappears or becomes shifted, indicating that the effects stem from the change in SWCNT bonding frequencies near the defect due to the change in the local charge distribution and resulting hybridization. This hypothesis is supported by previous work on π-orbital mismatch,[1,10] which demonstrates that the nearby bonds are deformed in such a way as to produce an increased mismatch between adjacent π-orbitals. This effect would also manifest itself in the resulting vibrational modes localized near the defect.

The sub-gap energy (Fig. 5d) for the (6,2) ortho(-) (red) shows similar characteristics in Fourier space as the NACT, which is expected since the NACT ~ $1/\Delta E$, although with additional noise for the 2CH$_3$ adduct especially. The dominant peak is found at 45 – 50 fs with a second near 55 – 60 fs. The inset shows a vertical log-scale. All species also exhibit a small peak near the 20-fs mode. For the NACT, the most similar to the two (6,2) ortho(-) species (red) is the (11,0) chirality (blue); although, it shows much weaker coupling to the two modes. In contrast, the two (6,2) ortho(++) species show significant delocalization across the Fourier space, exhibiting a very weak peak around 40 – 45 fs. In this case, the peak at 55 fs disappears completely for both the 2CH$_3$ and 2F adducts, indicating that the change in configuration decoupled the NACT from the higher-period mode. Strangely, the (6,5) SWCNT contains only a single peak at 20 fs. All species have a small peak at this frequency, which is expected to stem from the carbon backbone of the SWCNT (Fig. S10a).

The sub-gap energy for (6,5) (Fig. 5d) also only couples to the 20-fs mode, while the other chiralities show significant peaks around 20 and 45 fs. All other species couple to the same two modes as in the NACT. This data indicates that the *(6,5) chirality provides NACT that are decoupled from both main modes seen in other functionalized SWCNT chiralities, supporting its slow population dynamics.*

In conclusion, we have explored the effects of topological sp^3-defects on the non-radiative relaxation dynamics in SWCNT systems between the band-edge E_{11} and defect-associated E_{11}^* excitons. Utilizing semi-empirical simulations that have been well-justified in similar systems[30,35,36] and configuration interaction (CIS) level accounting for excitonic effects, SWCNTs of more than 300 atoms were modeled, which, to our knowledge, is the largest non-adiabatic dynamics simulation at this level to date. We have routed out structure-property correspondence between the defect's chemical composition and topological configuration as well as between SWCNT chiralities. To our surprise, the chemical composition of the sp^3-defect was largely responsible for the resulting population relaxation rate, showing that the electronegative fluorine adducts cause a large redistribution of charges near the defect site compared to that of methyl adducts. As such, all properties controlling the relaxation (i.e., the non-adiabatic coupling scalars) are modified.

In a recent report, we have discussed that one can achieve a reasonably large tunability in redshift purely from the chemical composition of the defect in *only* the most redshifted configuration.[7] However, for the dynamical situation presented here, it seems that the composition of the defect plays a larger role in determining the excitonic relaxation than its configuration, in stark contrast to expectations. This is *an extremely relevant finding* that showcases an important instance where one needs move past the "static picture" for these systems in order to rationalize experimental results on time-resolved excitonic dynamics.

It should be noted that the time constants produced here are not directly comparable to the bi-exponential decay fits of recent works[5,14], as the systems in this work are extremely short (2–3 nm) and exhibit only a single defect-associated state below the E_{11} exciton. However, the information stored in the time constants here can be interpreted qualitatively as a measure of the electronic coupling between the bright emitting state E_{11}^* and the higher-energy E_{11} in experiment, which gives information on the relaxation dynamics. This information is vital to adapt these systems for use in spintronic applications – where our results suggest that functionalizing low-chiral angle SWCNTs with strongly electronic withdrawing groups such as 2F provide quick decay into the quasi-two-state sub-system $\{S_0, S_1\}$.

Finally, our data suggests that the reorganization energy between excited states is large due to the charge redistribution on the surface, and so the commonly used "classical path approximation" would not be able to correctly simulate the dynamics of the realistic system. These approximations would neglect any changes in nuclear coordinates (i.e., forces) stemming from the excited state surfaces, which, in the systems presented in this

work, would lead to increased coherence to excited states due to the inability of the system to properly relax into the S_1 minima.

Thus, this work shows that direct atomistic non-adiabatic dynamics simulations deliver important insights into excitonic dynamics of chemically functionalized carbon nanotubes. In our future studies, we will address (I) the effects of various normal modes on the reorganization energy to elucidate the important contributions from the geometric rearrangement between excited states, (II) the effects of π-orbital mismatch on the non-adiabatic coupling, (III) excitonic localization and its time-dependent correlations with the non-adiabatic coupling, (IV) interacting defect systems to showcase dynamical motion of the exciton between the coupled, deep potential energy wells.

Supporting Information

Contained in the supporting document are additional figures that demonstrate convergence of the dynamics and figure that aid in the explanation of the main points, followed by a section on the computational methods.

Acknowledgements

References

(1)   Gifford, B. J.; He, X.; Kim, M.; Kwon, H.; Saha, A.; Sifain, A. E.; Wang, Y.; Htoon, H.; Kilina, S.; Doorn, S. K.; Tretiak, S. Optical Effects of Divalent Functionalization of Carbon Nanotubes. *Chem. Mater.* **2019**, *31* (17), 6950–6961.

(2)   Gifford, B. J.; Kilina, S.; Htoon, H.; Doorn, S. K.; Tretiak, S. Exciton Localization and Optical Emission in Aryl-Functionalized Carbon Nanotubes. *J. Phys. Chem. C* **2018**, *122* (3), 1828–1838.

(3)   Gifford, B. J.; Saha, A.; Weight, B. M.; He, X.; Ao, G.; Zheng, M.; Htoon, H.; Kilina, S.; Doorn, S. K.; Tretiak, S. Mod(n-m,3) Dependence of Defect-State Emission Bands in Aryl-Functionalized Carbon Nanotubes. *Nano Lett.* **2019**, *19* (12), 8503–8509.

(4)   He, X.; Gifford, B. J.; Hartmann, N. F.; Ihly, R.; Ma, X.; Kilina, S. V.; Luo, Y.; Shayan, K.; Strauf, S.; Blackburn, J. L.; Tretiak, S.; Doorn, S. K.; Htoon, H. Low-Temperature Single Carbon Nanotube Spectroscopy of Sp[3] Quantum Defects. *ACS Nano* **2017**, *11* (11), 10785–10796.

(5)   He, X.; Sun, L.; J. Gifford, B.; Tretiak, S.; Piryatinski, A.; Li, X.; Htoon, H.; K. Doorn, S. Intrinsic Limits of Defect-State Photoluminescence Dynamics in Functionalized Carbon Nanotubes. *Nanoscale* **2019**, *11* (18), 9125–9132.

(6)   Kwon, H.; Furmanchuk, A.; Kim, M.; Meany, B.; Guo, Y.; Schatz, G. C.; Wang, Y. Molecularly Tunable Fluorescent Quantum Defects. *J. Am. Chem. Soc.* **2016**, *138* (21), 6878–6885.

(7)   Weight, B. M.; Gifford, B. J.; Tretiak, S.; Kilina, S. Interplay between Electrostatic Properties of Molecular Adducts and Their Positions at Carbon Nanotubes. *J. Phys. Chem. C* **2021**, *125* (8), 4785–4793.

(8)   Settele, S.; Berger, F. J.; Lindenthal, S.; Zhao, S.; El Yumin, A. A.; Zorn, N. F.; Asyuda, A.; Zharnikov, M.; Högele, A.; Zaumseil, J. Synthetic Control over the Binding Configuration of Luminescent Sp 3 -Defects in Single-Walled Carbon Nanotubes. *Nature Communications* **2021**, *12* (1), 2119.

(9)   Lohmann, S.-H.; Trerayapiwat, K. J.; Niklas, J.; Poluektov, O. G.; Sharifzadeh, S.; Ma, X. Sp3-Functionalization of Single-Walled Carbon Nanotubes Creates Localized Spins. *ACS Nano* **2020**, *14* (12), 17675–17682.

(10)   Gifford, B. J.; Kilina, S.; Htoon, H.; Doorn, S. K.; Tretiak, S. Controlling Defect-State Photophysics in Covalently Functionalized Single-Walled Carbon Nanotubes. *Acc. Chem. Res.* **2020**, *53* (9), 1791–1801.

(11)   Kilina, S.; Ramirez, J.; Tretiak, S. Brightening of the Lowest Exciton in Carbon Nanotubes via Chemical Functionalization. *Nano Lett.* **2012**, *12* (5), 2306–2312.

(12)   Weight, B. M.; Sifain, A. E.; Gifford, B. J.; Kilin, D.; Kilina, S.; Tretiak, S. Coupling between Emissive Defects on Carbon Nanotubes: Modeling Insights. *J. Phys. Chem. Lett.* **2021**, *12* (32), 7846–7853.

(13)   Zheng, Y.; Bachilo, S. M.; Weisman, R. B. Controlled Patterning of Carbon Nanotube Energy Levels by Covalent DNA Functionalization. *ACS Nano* **2019**, *13* (7), 8222–8228.

(14)   Zheng, Y.; Weight, B. M.; Jones, A. C.; Chandrasekaran, V.; Gifford, B. J.; Tretiak, S.; Doorn, S. K.; Htoon, H. Photoluminescence Dynamics Defined by Exciton Trapping Potential of Coupled Defect States in DNA-Functionalized Carbon Nanotubes. *ACS Nano* **2021**, *15* (1), 923–933.

(15)   Zheng, Y.; Kim, Y.; Jones, A. C.; Olinger, G.; Bittner, E. R.; Bachilo, S. M.; Doorn, S. K.; Weisman, R. B.; Piryatinski, A.; Htoon, H. Quantum Light Emission from Coupled Defect States in DNA-Functionalized Carbon Nanotubes. *ACS Nano* **2021**, *15* (6), 10406–10414.

(16)   Endo, T.; Ishi-Hayase, J.; Maki, H. Photon Antibunching in Single-Walled Carbon Nanotubes at Telecommunication Wavelengths and Room Temperature. *Appl. Phys. Lett.* **2015**, *106* (11), 113106.

(17)   Jeantet, A.; Chassagneux, Y.; Raynaud, C.; Roussignol, Ph.; Lauret, J. S.; Besga, B.; Estève, J.; Reichel, J.; Voisin, C. Widely Tunable Single-Photon Source from a Carbon Nanotube in the Purcell Regime. *Phys. Rev. Lett.* **2016**, *116* (24), 247402.

(18)   Kryjevski, A.; Mihaylov, D.; Kilina, S.; Kilin, D. Multiple Exciton Generation in Chiral Carbon Nanotubes: Density Functional Theory Based Computation. *J. Chem. Phys.* **2017**, *147* (15), 154106.

(19)   Kryjevski, A.; Gifford, B.; Kilina, S.; Kilin, D. Theoretical Predictions on Efficiency of Bi-Exciton Formation and Dissociation in Chiral Carbon Nanotubes. *J. Chem. Phys.* **2016**, *145* (15), 154112.

(20)   Hyeon-Deuk, K.; Prezhdo, O. V. Time-Domain Ab Initio Study of Auger and Phonon-Assisted Auger Processes in a Semiconductor Quantum Dot. *Nano Lett.* **2011**, *11* (4), 1845–1850.

(21)   Pal, S.; Casanova, D.; Prezhdo, O. V. Effect of Aspect Ratio on Multiparticle Auger Recombination in Single-Walled Carbon Nanotubes: Time Domain Atomistic Simulation. *Nano Lett.* **2018**, *18* (1), 58–63.

(22)   Lüer, L.; Hoseinkhani, S.; Polli, D.; Crochet, J.; Hertel, T.; Lanzani, G. Size and Mobility of Excitons in (6, 5) Carbon Nanotubes. *Nature Phys* **2009**, *5* (1), 54–58.

(23)   Perebeinos, V.; Tersoff, J.; Avouris, P. Mobility in Semiconducting Carbon Nanotubes at Finite Carrier Density. *Nano Lett.* **2006**, *6* (2), 205–208.

(24)   Postupna, O.; Jaeger, H. M.; Prezhdo, O. V. Photoinduced Dynamics in Carbon Nanotube Aggregates Steered by Dark Excitons. *J. Phys. Chem. Lett.* **2014**, *5* (21), 3872–3877.

(25)   Amori, A. R.; Hou, Z.; Krauss, T. D. Excitons in Single-Walled Carbon Nanotubes and Their Dynamics. *Annual Review of Physical Chemistry* **2018**, *69* (1), 81–99.

(26)   Laird, E. A.; Pei, F.; Kouwenhoven, L. P. A Valley–Spin Qubit in a Carbon Nanotube. *Nature Nanotech* **2013**, *8* (8), 565–568.

(27)   Cubaynes, T.; Delbecq, M. R.; Dartiailh, M. C.; Assouly, R.; Desjardins, M. M.; Contamin, L. C.; Bruhat, L. E.; Leghtas, Z.; Mallet, F.; Cottet, A.; Kontos, T. Highly Coherent Spin States in Carbon Nanotubes Coupled to Cavity Photons. *npj Quantum Information* **2019**, *5* (1), 1–5.

(28)   Piao, Y.; Meany, B.; Powell, L. R.; Valley, N.; Kwon, H.; Schatz, G. C.; Wang, Y. Brightening of Carbon Nanotube Photoluminescence through the Incorporation of Sp 3 Defects. *Nat. Chem.* **2013**, *5* (10), 840–845.

(29)   Malone, W.; Nebgen, B.; White, A.; Zhang, Y.; Song, H.; Bjorgaard, J. A.; Sifain, A. E.; Rodriguez-Hernandez, B.; Freixas, V. M.; Fernandez-Alberti, S.; Roitberg, A. E.; Nelson, T. R.; Tretiak, S. NEXMD Software Package for Nonadiabatic Excited State Molecular Dynamics Simulations. *J. Chem. Theory Comput.* **2020**, *16* (9), 5771–5783.

(30)   Sifain, A. E.; Bjorgaard, J. A.; Nelson, T. R.; Nebgen, B. T.; White, A. J.; Gifford, B. J.; Gao, D. W.; Prezhdo, O. V.; Fernandez-Alberti, S.; Roitberg, A. E.; Tretiak, S. Photoexcited Nonadiabatic Dynamics of Solvated Push–Pull π-Conjugated Oligomers with the NEXMD Software. *J. Chem. Theory Comput.* **2018**, *14* (8), 3955–3966.

(31)   Tully, J. C. Molecular Dynamics with Electronic Transitions. *J. Chem. Phys.* **1990**, *93* (2), 1061–1071.

(32)   Englman, R.; Jortner, J. The Energy Gap Law for Radiationless Transitions in Large Molecules. *Molecular Physics* **1970**, *18* (2), 145–164.

(33)   Shreve, A. P.; Haroz, E. H.; Bachilo, S. M.; Weisman, R. B.; Tretiak, S.; Kilina, S.; Doorn, S. K. Determination of Exciton-Phonon Coupling Elements in Single-Walled Carbon Nanotubes by Raman Overtone Analysis. *Phys. Rev. Lett.* **2007**, *98* (3), 037405.

(34)   Yin, Y.; Vamivakas, A. N.; Walsh, A. G.; Cronin, S. B.; Ünlü, M. S.; Goldberg, B. B.; Swan, A. K. Optical Determination of Electron-Phonon Coupling in Carbon Nanotubes. *Phys. Rev. Lett.* **2007**, *98* (3), 037404.

(35)   Dreuw, A.; Head-Gordon, M. Single-Reference Ab Initio Methods for the Calculation of Excited States of Large Molecules. *Chem. Rev.* **2005**, *105* (11), 4009–4037.

(36)   Ondarse-Alvarez, D.; Nelson, T.; Lupton, J. M.; Tretiak, S.; Fernandez-Alberti, S. Let Digons Be Bygones: The Fate of Excitons in Curved π-Systems. *J. Phys. Chem. Lett.* **2018**, *9* (24), 7123–7129.